Surface & Coatings Technology 436 (2022) 128306

Contents lists available at ScienceDirect

Surface & Coatings Technology

journal homepage: www.elsevier.com/locate/surfcoat

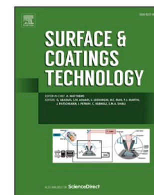

Niobium thin film thickness profile tailoring on complex shape substrates using unbalanced biased High Power Impulse Magnetron Sputtering

Guillaume Rosaz *, Aleksandra Bartkowska [1], Carlota P.A. Carlos, Thibaut Richard, Mauro Taborelli

CERN, European Organization for Nuclear Research, 1211 Geneva 23, Switzerland

A R T I C L E I N F O

Keywords:
HiPIMS
Superconducting radiofrequency cavity
Niobium thin film
Particle in cell Monte Carlo simulation
Unbalanced magnet
Thickness profile distribution

A B S T R A C T

The authors report in this paper the possibility to control the thickness profile of a thin film deposited by High Power Impulse Magnetron Sputtering (HiPIMS). It is shown that the combination between a HiPIMS discharge, an unbalanced magnetic configuration and the application of a negative bias onto the surface to coat enables tailoring on demand the coating thickness profile. This effect is hereafter used to coat complex shapes such as low-beta accelerating cavities with a niobium layer. The authors first present the magnetic design proposed to obtain an unbalanced cylindrical sputtering source. Numerical simulations are then used to predict the electron density and energy spatial distributions that can subsequently be correlated to the ionization region shape. Finally, the authors present the effect of such technique comparing Direct Current Magnetron Sputtering (DCMS), HiPIMS and biased HiPIMS using, respectively, a balanced and an unbalanced magnetic configuration, as well as detailing the effect of modifying either the magnetic field lines distribution or the magnetic strength.

1. Introduction

Niobium coated copper (Nb/Cu) superconducting radiofrequency (SRF) cavities are a promising alternative to bulk niobium ones. They have been used at CERN since the Large Electron Positron (LEP) collider [1] [2] and continue to be used for the Large Hadron Collider (LHC) [3], as well as for HIE-ISOLDE [4] [5] facility and in other institutes such as SOLEIL synchrotron [6]. However, despite their clear advantages in the 80's over bulk Nb, the strong R&D carried out on bulk niobium cavities pushed the latter's performance [7] far beyond what Nb/Cu has ever been capable of.

The main drawback of coated cavities lies in the so-called Q-slope phenomenon that results in an exponential decrease of the cavities' quality factor, Q, when increasing the available accelerating field [8]. The precise origin of this decrease still remains unclear, but some causes have been identified, the major one being the porosities of the thin film that appear during the growth due to the sputtering technique itself [9]. Indeed, the cavities are coated using Direct Current Magnetron Sputtering (DCMS) as it allows working with an ultrapure base material, which is a pre-requisite to achieve high quality superconducting performance. However, the films elaborated with this technique are subject to shadowing effects and the method itself leads to non-conformal layers. SRF cavities have meter size complex shapes, which results in the presence of voids in areas that do not face the target directly. This particular effect was studied in depth using different elliptical cavity shapes [10] [11]. In DCMS, the coating profile is peaked close to the cavity's iris (as defined in Fig. 1) due to its proximity to the cathode. It has been shown [12] that a minimum Nb thickness is required at the cavity's equatorial plane to guarantee a proper electromagnetic shielding during operation. To achieve such a thickness, the price to pay is a very thick layer close to the iris, which is prone to enhance interface stress and provoke adhesion problems. As those cavities are subject to high pressure water rinsing (HPWR) [12], this may result in layer peel-off in this specific area.

In this work, we propose to investigate suitable balanced and unbalanced magnetic configurations with a magnetron sputtering source in order to control the thickness profile over the complex shape of an accelerating cavity. Previous works have already pointed out such a possibility using circular planar magnetrons [13] [14]. In our case, the challenge lies in the cylindrical geometry of the sputtering target. We will thus discuss the design of unbalanced magnetic assemblies, evaluate how they influence the shape of the ionization region and the overall

* Corresponding author.
E-mail address: Guillaume.rosaz@cern.ch (G. Rosaz).
[1] Present address: Departament de Física, Universitat Autònoma de Barcelona, 08193, Bellaterra, Spain.

https://doi.org/10.1016/j.surfcoat.2022.128306
Received 11 January 2022; Received in revised form 9 February 2022; Accepted 25 February 2022
Available online 4 March 2022
0257-8972/© 2022 The Author(s). Published by Elsevier B.V. This is an open access article under the CC BY license (http://creativecommons.org/licenses/by/4.0/).

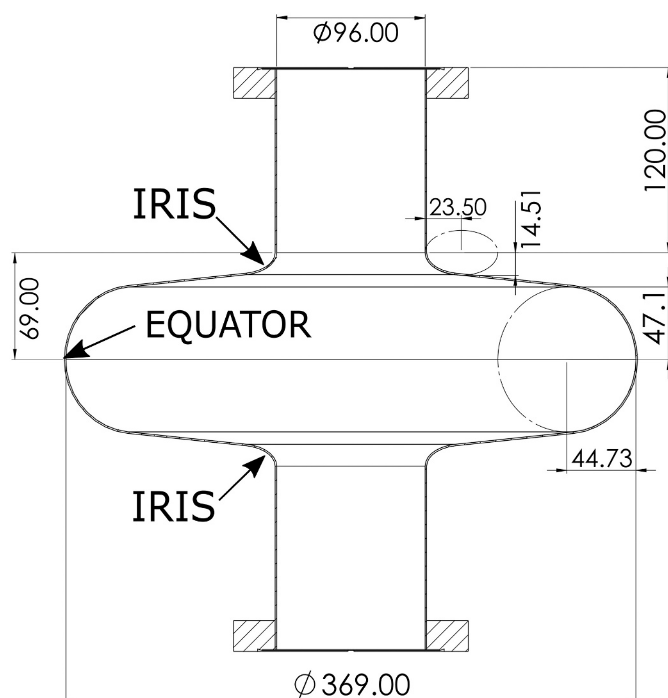

Fig. 1. Schematic drawing of a 704 MHz, β = 0.65 accelerating cavity. Dimensions are given in mm.

coating profile.

In the following, we will first describe how different field configurations were set-up in a cylindrical geometry. A second section illustrates how the resulting magnetic field maps were calculated and measured at specific profile lines for benchmarking in order to assess a solid basis for the interpretation and further designs. The plasma discharges are then simulated accordingly to outline the different behaviours of our magnetic configurations. The magnetic configurations are then tested in DCMS mode to compare the experimental coating profiles to the simulated ones. Then, we report on the effect of the two magnetic configurations using a highly ionized discharge by means of High Power Impulse Magnetron Sputtering (HiPIMS). After pointing out the interest of using such a discharge, we demonstrate that the use of an active DC biasing voltage on the substrate combined to a HiPIMS discharge leads to significant coating profile modifications depending on the magnetic assembly configuration. Based on these observations, we then study in two separated times the impact of the magnetic field distribution and strength onto the coating distribution.

2. Experimental setup

In this work, a 704 MHz elliptical copper cavity with a beta factor (defined as the ratio of the particles speed over the speed of light) of 0.65 was used as a substrate, as presented in Fig. 1. This cavity is well suited to the purpose of this study for the two following reasons. First, the slope of the cavity walls is about 84° with respect to the cavity axis and is well suited for studying the layer densification. The second interest of this object lies in the diameter difference of the cut-offs and cell. As the sputtering cathode has to be inserted by the cut-offs, its size will necessarily be inappropriate for coating efficiently the equatorial plane. Any impact of a process parameter onto the coating rate of the equator will then be easier to track as reported later on in this study.

An oxygen-free copper stripe that follows the cavity internal shape has been inserted in order to perform thickness measurements of the deposited thin film over the entire shape of the cavity cell. The stripe is plastically deformed using two stainless steel dyes made to reproduce the cavity shape and is maintained in place thanks to two stainless steel rings placed in the cut-offs.

The niobium thin films were deposited using an apparatus shown in Fig. 2. The cavity (Fig. 2 (4)) is mounted around a cylindrical cathode (Fig. 2 (1)) and insulated from it and from the ground using two ceramic vacuum breaks (Fig. 2, (2a) and (2b)). Two small chambers equipped with a CF-DN16 port (Fig. 2, (3a) and (3b)) are used to connect the hereafter described anodes. A DN40 port is used on the lower chamber (Fig. 2 (3b)) to connect a non-evaporable getter (NEG) pump. At the extremity, an angle valve (Fig. 2 (5)) does the connection to the ultra-high vacuum pumping group, also equipped with injection valves for the process gas. Fig. 2 b) shows a cross section view of the setup. The inset, Fig. 2 c), highlights the cathode assembly. The latter is made of a 38 mm external diameter stainless steel tube (Fig. 2 (7), highlighted in green), closed at its lower extremity and welded to the cathode top flange (Fig. 2 (1)). A central cylindrical electrode, made of pure Nb with 45 mm external diameter (Fig. 2 (10), highlighted in dark blue), is in direct contact with the stainless steel tube. Two cylindrical Al_2O_3 ceramics (Fig. 2 (8), highlighted in red) are used as electrical insulators between the central tube and the upper and lower electrodes (Fig. 2, (9a) and (9b) respectively, highlighted in light blue). These electrodes, of 53 mm external diameter, are also made of pure niobium. The upper and lower electrodes are electrically connected using type-N UHV connectors (Fig. 2 (6a) and (6b) respectively). The three electrodes can thus be independently connected either to a power supply or to the ground. This is of special interest when coating the full cavity. To coat the tubular parts of the cavity, namely the cut-offs, the three electrodes are cabled to the power supply and the cavity is kept at the ground potential. When coating the cavity cell, the central electrode is connected to the power supply, the upper and lower electrodes are kept at ground potential and the cavity can be biased at any desired potential. The upper and lower electrodes act as anodes and allow the electron current to flow out of the system during the plasma discharge. The magnetic field necessary for sustaining a magnetron discharge is provided by a cylindrical permanent NdFeB (N45SH) magnet (Fig. 2, (11)) whose typical dimensions are 50 mm in length, 30 mm external diameter and 10 mm internal diameter. The latter is held by a stainless steel tube (Fig. 2 (12)). A flow of compressed air in the tube cools down the magnet and prevents its demagnetization during the coating process.

Further in this study we will show the interest of using an active DC biasing voltage on the substrate in order to densify the coated layer. For that purpose the Cu cavity was replaced by a stainless steel chamber of similar dimensions that can house sample holders. This home-made sample holder is depicted in Fig. 3. On this holder, samples can be mounted at various angles with respect to the cathode surface (0, 45 and 90°).

3. Sample preparation and coating parameters

Prior to coating, the copper stripe is chemically degreased using a commercial detergent bath, then etched in a tri-acid mixture (H_2SO_4 42% vol, HNO_3 8% vol, HCl 0.2% vol) and passivated in a sulphochromic acid bath. Afterwards, it is rinsed with demineralized water and ultrapure alcohol, followed by dry-air blowing. The sample is then mounted in the cavity and the coating setup is assembled in a cleanroom.

The cavity is pumped down to about 1.10^{-7} mbar and a leak check is performed. Then, the pumping group, the coating apparatus and the cavity are baked out at 200 °C for 48 h. Before stopping the bakeout everywhere except in the cavity that is maintained at 200 °C, the NEG pump is activated for 4 h. When cooled down, the whole setup reaches a base pressure of about 6×10^{-10} mbar. Ultra-pure krypton is then injected by means of a leak valve to reach a process pressure of 2.3×10^{-3} mbar. During the coating process, the cavity temperature is monitored using an infrared thermal sensor and kept constant at 150 °C with a fan.

The plasma discharge is maintained using a Huettinger TruPlasma HighPulse 4006 power supply and monitored using a high voltage probe

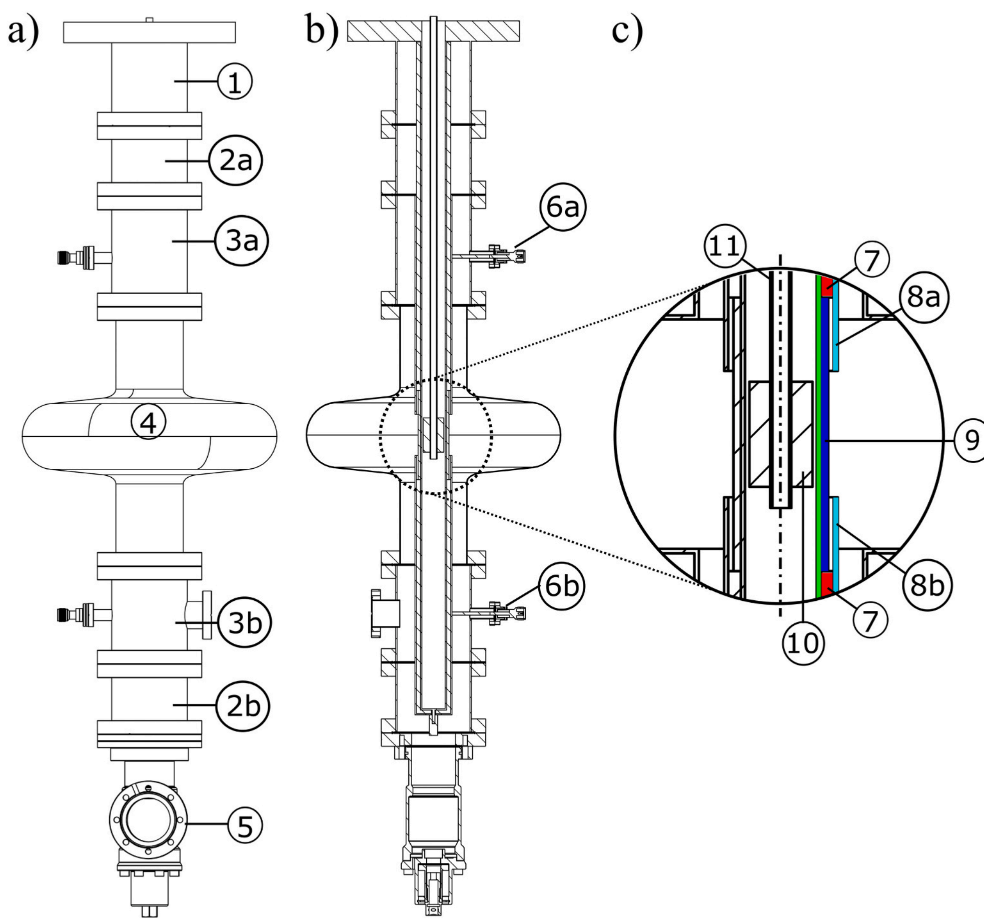

Fig. 2. a) Schematic representation and b) cross section view of the coating apparatus used to deposit Nb into SRF cavities. The inset c) highlights the cathode assembly. 1 is the cathode support, 2a and 2b are the upper and lower ceramic spacers respectively. 3a and 3b are the upper and lower chambers supporting the anodes connexions respectively. 4 is the cavity. 5 is the angle for connexion to the pumping group. 6a and 6b are the upper and lower anode electrical connectors respectively. 7 is the ceramic to insulate the cathode from the anodes. 8a and 8b are the upper and lower anodes respectively. 9 is the Nb cathode. 10 is the permanent magnet. 11 is the support and cooling rod for the permanent magnet.

(Tektronix P6015A) and a current probe (Pearson current monitor 301×). When needed, a negative bias voltage is applied to the cavity using a TruPlasma Bias 3018 power supply whose current is also monitored with a Pearson current monitor 301×. The probes signals are recorded with a digital oscilloscope Picoscope 2000. DCMS and HiPIMS discharges are kept at a constant average power of about 1.3 kW. The HiPIMS pulse is 200 μs long with a repetition frequency of 100 Hz. DCMS and HiPIMS coatings are performed over a total duration of 1 h and 1 h30, respectively, to ensure a sufficiently thick layer for proper characterization.

The Nb layer thickness is measured by X-ray fluorescence using the attenuation method. A measurement point is taken every 2 mm along the unfolded copper.

A Zeiss Sigma field emission gun Scanning Electron Microscope (SEM), equipped with an InLens detector (Secondary Electron), an Everhart-Thornley secondary electron detector and a backscattered electron detector, was used for imaging.

To examine the cross section of the films, a ZEISS 'XB540' focused ion beam (FIB) was used. For the cross sectional milling, Pt deposition on top of the film was initially performed at a milling current of 300 pA and an accelerating voltage of 30 kV to deposit a 1 × 3 × 15 μm^3 protection barrier. Coarse milling at a current of 7 nA and accelerating voltage of 30 kV was then used to remove a 5 × 7 × 20 μm^3 region of material, before polishing the cross sectional surface at a mild milling current of 300 pA.

4. Simulation methods

Magneto-static simulations were performed using the Finite Element Method Magnetics (FEMM) package [15]. This package was used to estimate the magnetic field at the cathode surface as well as the field distribution in the cavity volume. Once the magnetic configurations are designed, we proceed to plasma simulations according to the following procedure.

Full 3D plasma simulations were performed on a high performance computing (HPC) cluster located at CERN with a Particle-in-Cell Monte Carlo (PICMC) parallel code [16]. The simulation model consists of the geometry described in Fig. 2 restricted to an axial length of 85 mm centred on the equatorial plane, thus including the whole cavity cell and the beginnings of the cut-offs, along with cathode and anodes.

The simulation workflow is divided into three steps. First, the magnetic field corresponding to each magnetic configuration described in Fig. 4 is computed on the three-dimensional simulation volume resorting to the Boundary Element Method (BEM). Then, the plasma discharges, for both magnetic cases described above, are modelled with the PICMC module of the code, providing both the plasma distribution and the erosion profile on the cathode. At last, neutral atom transport simulations using the Direct Simulation Monte Carlo (DSMC) module are run to obtain the niobium deposition profiles on the cavity surface. Relevant numerical and physical parameters used in the PICMC and DSMC simulations are listed in Table 1.

In the simulations, the X axis corresponds to the cavity axis. The 3D Cartesian volume mesh is refined in the 60 mm along the X direction corresponding to the denser plasma region with a size of 0.5 mm, while keeping it at 1 mm in the rest of the volume and in the other directions. The initial krypton process pressure is identical to the experimental one, i.e. $p_{Kr} = 2.3 \times 10^{-3}$ mbar, and is maintained through the simulation run by constant boundary conditions at both cut-offs' extremities. Scaling factors for the different species correspond to the ratios between real number of physical particles and simulated macro-particles, and are

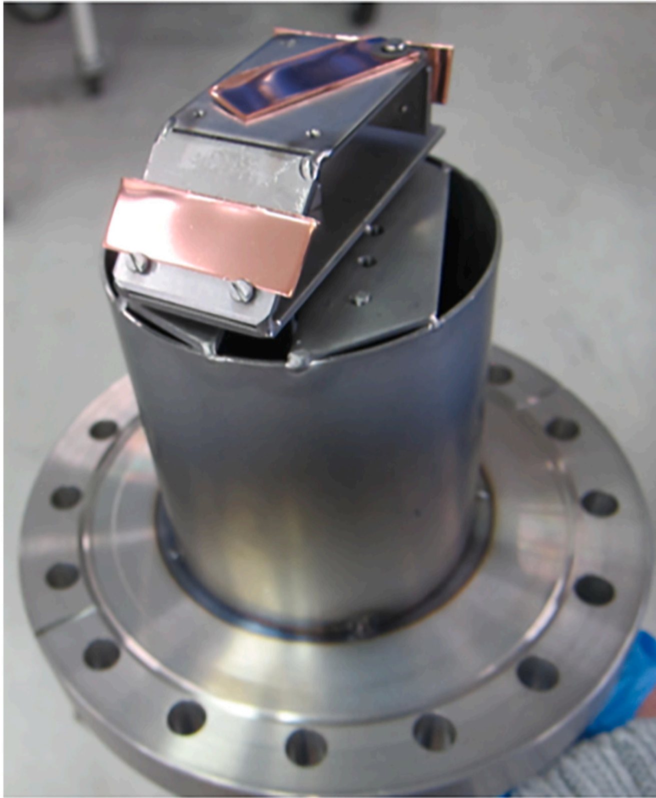

Fig. 3. Sample holder used for mounting three copper samples at various angles with respect to the cathode surface.

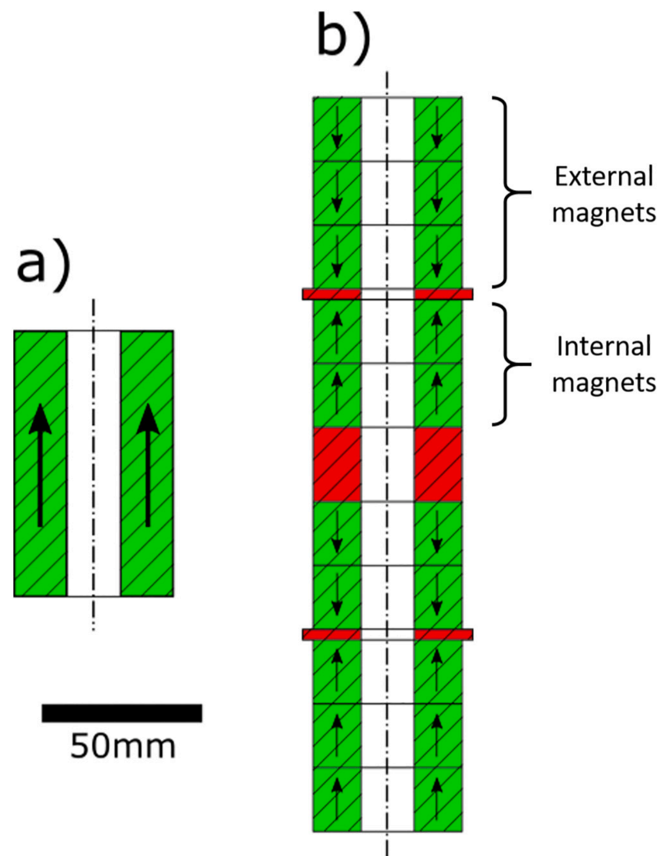

Fig. 4. Cross-section views of the magnets used in this study: a) cylindrical NdFeB magnet and b) unbalanced 3-2-14 mm-SmCo configuration, consisting of a pile-up of SmCo magnets (green) and iron poles (red). The arrows indicate the magnetization orientation.

chosen to ensure sufficient statistics in each simulation cell for the volume collision reactions. Ion-induced secondary electron emission (IISEE) is modelled according to [17], by adapting the yield γ_{IISEE} and energy distribution to Kr^+ bombardment on niobium instead of Ar^+. Volume reactions are taken from the code library and include momentum transfer between neutral particles, momentum transfer and excitation between electrons and krypton atoms, momentum transfer between krypton ions and atoms, and ionization.

The simulated discharge power P_{dis} is restricted to 10 W, which is significantly lower than the experimental one. This difference is motivated by numerical constraints in terms of time step, mesh size and computational cost which would render higher power simulations, characterized by higher currents and densities of charged particles, impossible to carry on. The present simulations aim at giving qualitative information in terms of plasma shaping due to different magnetic configurations and their respective influence on thin film thickness profiles, which are not severely impacted by the discharge power.

In the PICMC simulation, krypton ions bombarding the cathode are sputtering niobium neutrals according to Yamamura's analytical formula [18], which depends on the bombarding ion energy. An output of the plasma simulations is therefore the profile of sputtered niobium atoms from the cathode. This profile can in turn be used as an input to the DSMC simulation, in which niobium atoms are sputtered away from the cathode according to a total flux and a 3D profile given by the plasma simulation, with a Thompson initial energy distribution and a power cosine of exponent 0.5 initial angle distribution. The flux of niobium atoms impinging on the cavity surface can then be converted into a deposition profile and compared to experimental results. For this comparison only the DCMS experimental data will be considered as the code cannot perform HiPIMS simulation.

The convergence of the PICMC simulations is defined as the moment when the discharge voltage and current are stable.

Table 1
Physical and numerical parameters used in the PICMC and DSMC simulations.

Parameter	Value
Domain size in XYZ [mm^3]	170 × 380 × 380
Mesh size in the plasma region [mm^3]	0.5 × 1 × 1
CPU used per run (cores)	100
Krypton pressure [mbar]	2.3×10^{-3} mbar
Scaling factor Krypton	1.4×10^{9}
PICMC parameters	
Discharge power P_{dis} [W]	10
Time step [s]	5×10^{-12}
Species	Kr, Kr^+, e^-, Nb
Scaling factor Kr^+, e^-	10^4
Initial density Kr^+, e^- [m^{-3}]	5×10^{12}
γ_{IISEE}	0.085
IISE energy distribution	Gaussian
IISE angular distribution	cosine
Electron capture probability on physical surfaces	100%
Sputtering yield	According to Yamamura's analytical formula [18]
Simulation time	~2 months
DSMC parameters	
Time step [s]	1×10^{-7}
Species	Kr, Nb
Scaling factor Nb	8×10^5
Nb initial energy distribution	Thompson
Nb initial angle distribution	cosine with exponent 0.5
Simulation time	~10 days

5. Simulations results

5.1. Magnetic simulations

Two magnetic configurations were simulated in order to evaluate the feasibility of building an unbalanced cylindrical magnetron. The first configuration, designated hereafter as the balanced configuration, consists of a cylindrical NdFeB (N45SH) magnet of 50 mm length, 30 mm external diameter and 10 mm internal diameter as shown in Fig. 4a). The field lines developed by such a magnet, calculated through FEMM, are shown in Fig. 5a).

The second magnetic configuration is designed to provide an unbalanced field while keeping the cylindrical symmetry. To do so, the proposed solution is as follows: ten cylindrical SmCo (Sm32/15–17) magnets (12 mm in length, 28 mm external diameter and 10 mm internal diameter) are arranged together as shown in Fig. 4 b), in combination with three pure iron cylinders. This type of assembly will henceforth be referred to as unbalanced X-Y-L-Material (X = number of external magnets, Y = number of internal magnets, L = length of the central iron pole in mm, Material = magnetic material), thus the label 3-2-14 mm-SmCo. The magnets are placed with opposed magnetization direction in order to provide the poles of the unbalanced arrangement.

In the same fashion as for the simple balanced configuration, 2D simulations were carried out to evaluate the field lines map of the unbalanced configuration. As shown on Fig. 5 b), the iron discs act as the magnetic poles of the assembly and redirect the field lines so that they intercept the cathode surface perpendicularly. We can note that this configuration exhibits a magnetic profile where some flux lines exiting the cathode surface intercept the substrate surface. By doing so, some electrons are allowed to travel toward the cavity's surface and thus extend the ionization region. This configuration may then provide the possibility to extend the flux of ionized metallic species closer to the surface to coat, and ultimately redistribute the coating profile when using HiPIMS discharge. This point will be assessed later in this paper.

In order to quantify the difference between the different magnetic configurations and based on the work of Svadkovski et al. [19], further studies for the estimation of the unbalanced magnetron parameters, which characterise the field configuration at the front of a target, were carried out. The coefficient of unbalance K can be expressed as:

$$K = \frac{\Phi_1}{\Phi_2} = \frac{\int_{S_1} B_{\perp 1} dS}{\int_{S_2} B_{\perp 2} dS}$$

where $B_{\perp 1}$ and S_1 are the component of the magnetic field perpendicular to the target surface and the cross-sectional area of the outer magnets, respectively, B_2 and S_2 are the component of the magnetic field perpendicular to the target surface and the cross-sectional area of the central magnets. We can also define a coefficient of geometrical unbalance K_G as:

$$K_G = Z_0 / 2\overline{R}$$

Where $\overline{R}$ is an average radius of the erosion zone and Z_0 is the distance from the target surface to the magnetic null point. The erosion zone is measured experimentally on the target and the magnetic null point is calculated based on the finite element simulations. The values obtained for each magnetic configuration are reported in Table 2. The peculiar configuration in balanced mode, using a single magnet, leads to a perfectly balanced configuration. In this case, the geometrical factor cannot be defined as no null point is present and the racetrack is perfectly centered, thus $\overline{R} = 0$ mm. Two other configurations are presented, 3–2-8 mm-SmCo and 3–2-8 mm-NdFeB, as they will be discussed in further sections. For now, however, the first two will remain the focus of this study.

The tangential component of the magnet's magnetic field was measured using a gaussmeter, as reported in Fig. 6a) and b) for the balanced NdFeB and unbalanced 3-2-14 mm-SmCo configurations, respectively. The probe was placed at 22 mm from the magnets surface in order to minimize the measurement error.

Overlaid with the experimental results in said figures are the data from the FEMM simulations for both configurations calculated using the magnetic properties communicated by the magnets' manufacturer. We notice that the experimental values are in good agreement with the predicted ones. With the finite element method being thus validated, the cathode surface total magnetic field profile was later estimated for both configurations, as reported in Fig. 6c).

To complete the definition and characterization of the magnetic assemblies, additional numerical plasma simulations were performed to evaluate if the ionization region can indeed be extended using the proposed unbalanced configuration

Table 2
Calculated unbalance coefficients for the different magnetic assemblies used in this study.

Magnetic configuration	K	K_G
Balanced - NdFeB	1	N/A
Unbalanced 3-2-14 mm-SmCo	2.32	0.9
Unbalanced 3-2-8 mm-SmCo	1.98	0.88
Unbalanced 3-2-8 mm-NdFeB	2.17	0.88

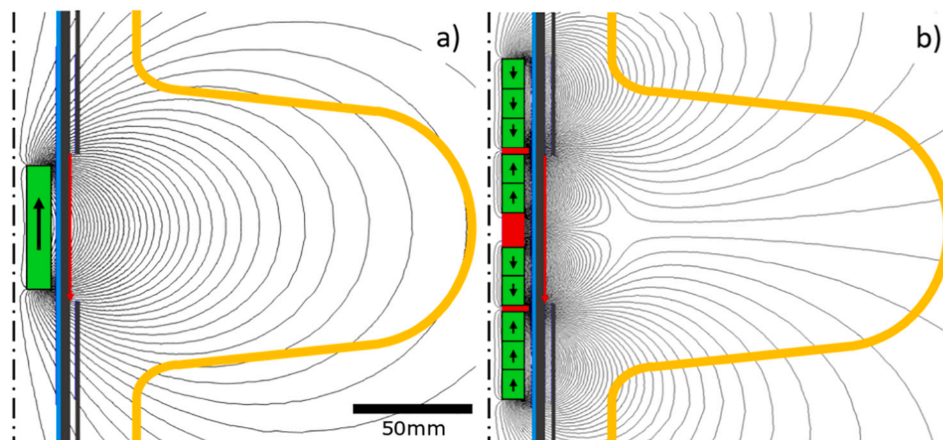

Fig. 5. Magneto-static simulations for the two magnetic configurations used in this study: a) balanced magnet and b) unbalanced 3-2-14 mm-SmCo magnet. The black arrows indicate the magnetization direction. The red arrow indicates the path along which the cathode surface field profile was evaluated.

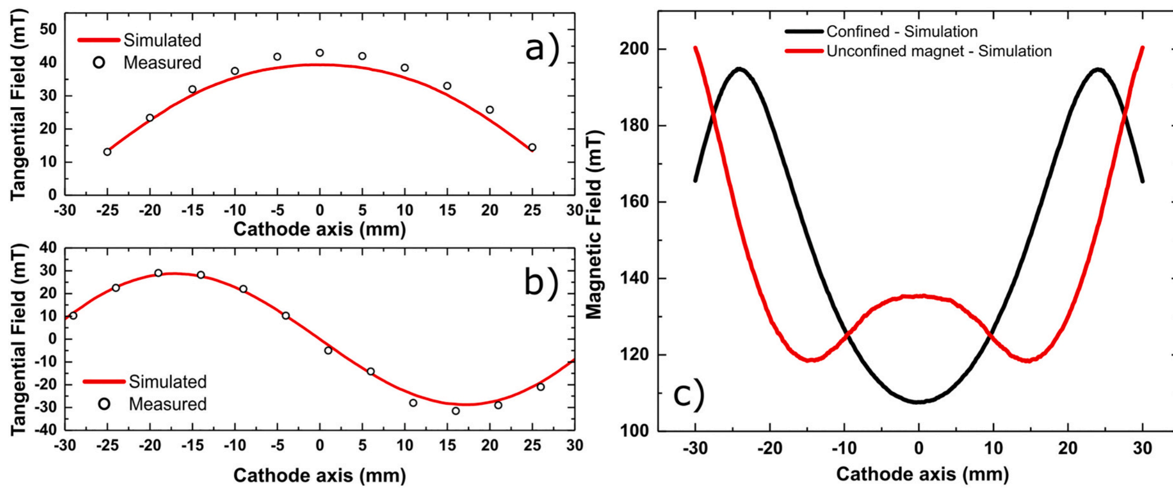

Fig. 6. Simulated and measured tangential magnetic fields for a) balanced configuration and b) unbalanced 3-2-14 mm-SmCo configuration, at 22 mm from the magnets surface. c) Simulated total magnetic strength profiles for both configurations at the cathode surface.

5.2. Plasma simulations

Plasma simulations for each magnetic configuration, balanced and unbalanced 3-2-14 mm-SmCo, were performed. Electron density spatial distributions for each converged simulation are shown Fig. 7, in the symmetry plane for the a) balanced case and b) the unbalanced one. Electrons mean energy profiles, spatially resolved at the simulation cell scale, are also reported on Fig. 7c) and d) for the same configurations, respectively.

The influence of the magnetic field configuration on the plasma distribution is clearly visible, since the balanced configuration (Fig. 7a)) is characterized by a single plasma ring located in the equatorial plane, with a maximum electron density close to the cathode and decaying toward the cavity surface. In the unbalanced 3-2-14 mm-SmCo configuration (Fig. 7b)), two plasma rings are located on each side of the equatorial plane, with a directed plasma plume in the equatorial plane, following the magnetic flux lines of Fig. 4 b) toward the cavity surface. The energy distribution also shows that energetic electrons are capable of reaching the equator using the unbalanced 3-2-14 mm-SmCo configuration, whereas in the balanced configuration the few electrons that arrive at the cavity surface are of very low energy. Therefore the unbalanced 3-2-14 mm-SmCo configuration is expected to provide a more extended region of ionization.

Niobium sputtering profiles, i.e. maps of the amount of sputtered atoms along the cathode surface, can be extracted from the plasma simulation. Such profiles are displayed in Fig. 8 after an azimuthal spatial averaging and a temporal averaging between 7 and 9 μs, corresponding to a stable plasma discharge in terms of voltage and current, and therefore a steady-state sputtering flux. The sputtering profile in the balanced magnetic case is clearly peaked in the equatorial plane, corresponding to the electron density maximum close to the cathode, while the unbalanced case is characterized by two peaks on each side of the equator plane, corresponding to the two plasma rings displayed in Fig. 7. The apparent asymmetry between the two peaks in the unbalanced case

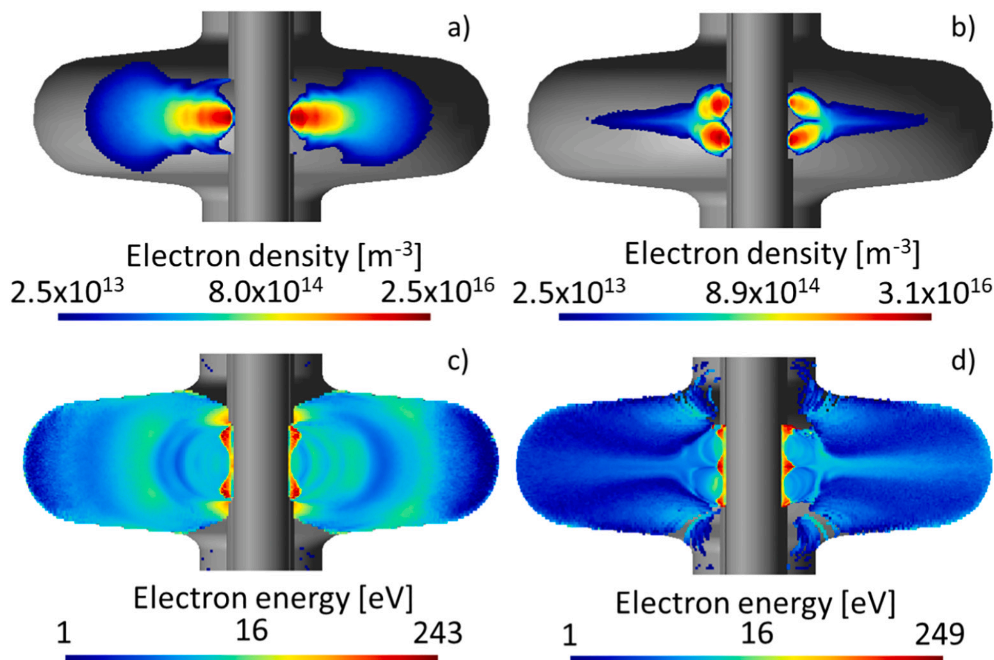

Fig. 7. Map of the electron density and electron energy in the symmetry plane for the balanced, a) and c), and unbalanced, b) and d), magnetic configurations at $t_{sim} = 9$ μs. Colour maps are displayed on a logarithmic scale.

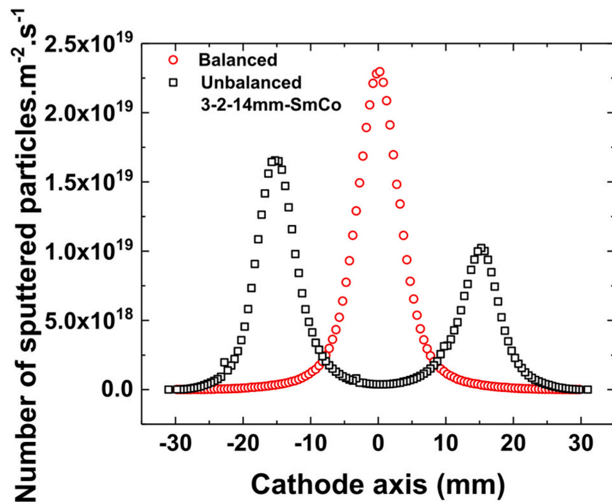

Fig. 8. Niobium sputtering profiles predicted by the PICMC simulations for the balanced assembly (red circles) and the unbalanced 3-2-14 mm-SmCo assembly (black squares).

is not clearly explained although it could be due to a random distribution fluctuation of charged particle densities between the two plasma rings at the short scale of the time average.

These sputtering profiles were used as inputs to the neutral transport simulation module, and the niobium deposition fluxes on the cavity surface were radially and time averaged between 30 and 50 ms to smoothen the results. The resulting thickness profiles projected on the cavity axis are presented in Fig. 9a) and compared with the experimental results. Two coatings in DCMS mode were performed using the two magnetic configurations. For direct comparison, all profiles are normalized to the thickness value obtained at the equatorial plane i.e., at 0 mm.

It clearly appears that the resulting film thickness profile is dictated by the distance of the cathode to the substrate as we observe peaked profile around the iris locations that are the closest to the cathode surface. This statement is supported by Fig. 9b), which represents the distance between the cavity surface and the cathode surface central point as a function of position along the cavity axis.

In spite of the different magnetic geometries, we notice that the coating profiles in balanced and unbalanced configurations are very similar. Indeed, in DCMS, the thin film thickness profile shape on the cavity surface is dominated by the transport of neutral sputtered niobium atoms through the krypton process gas phase. Even though the sputtering profiles at the cathode are significantly different between the balanced and unbalanced magnetic configurations, the number of racetracks does not seem to have any importance in the final film thickness distribution. It can be easily understood from a simple geometrical point of view, because the distances between the cavity surface and the cathode (displayed in Fig. 9b) are much larger than the distance separating the two racetrack rings in the unbalanced configuration (~30 mm, as seen in Fig. 8). In our low pressure regime where collisions in the gas phase are scarce, each racetrack contributes in an equivalent fashion to the total niobium flux arriving at the substrate in the unbalanced mode. The simulation correctly predicts the coating profiles starting from the two very different sputtering profiles. The slight differences that can be observed, especially concerning the peak around 70 mm, are attributed to the limit of accuracy by positioning the stripe within the cavity. Indeed, the sample stripe is only held in two points in the cut-offs and matches the cavity shape thanks to its elastic behaviour. We have seen that the stripe can be off from the surface by few millimetres.

This demonstrates that tuning the coating profile of a thin film in DCMS requires much more drastic changes as, for example, the modification of the cathode shape, which in our case is limited by the available aperture to introduce it into the cavity. For this reason, we investigated the application of a HiPIMS discharge in order to tune the coating profile on the substrate. The reference for comparison along the following part of this article will be the balanced DCMS coating result.

6. Influence of magnetic configuration in HiPIMS Coatings

6.1. Grounded substrate

We first started by performing HiPIMS coatings without applying any bias on the substrate using the two different magnetic configurations, to establish whether a fundamental difference would arise with respect to the DCMS discharge. The voltage and current curves as well as the thickness profiles are presented in Fig. 10 and Fig. 11, respectively.

The first noticeable point is the coating rate difference between the three configurations. As expected, the HiPIMS mode has a much lower coating rate due to an enhanced recapture rate of the metallic ions at the cathode surface, as explained in previous studies [20]. The use of an unbalanced 3-2-14 mm-SmCo source leads to a reduction of the coating rate with respect to the balanced configuration by a factor of 2.6 ± 0.9 in average. One can explain this by the fact that for a given power, the ion density close to the cathode surface is reduced due to the extended production toward the cavity's surface as shown in the simulation on

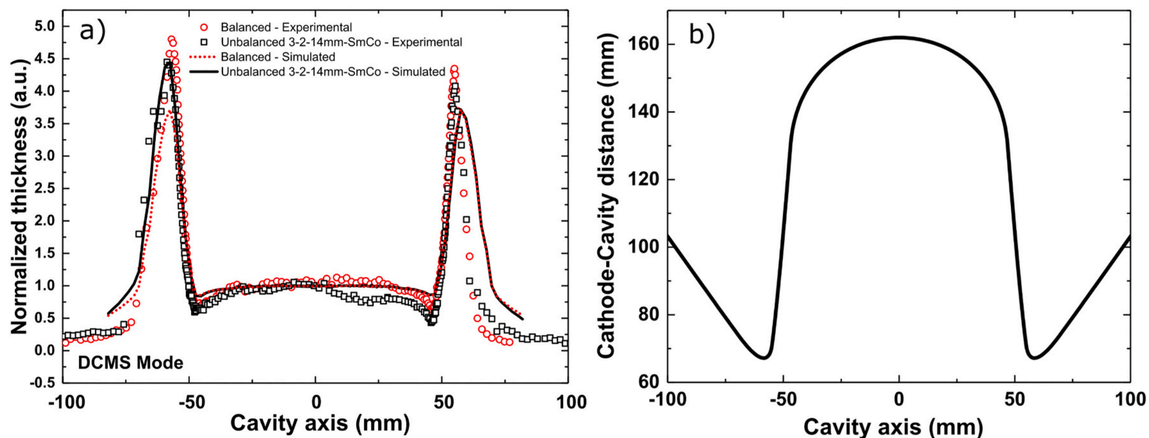

Fig. 9. a) Normalized thickness profiles of Nb coatings performed on a low beta 704 MHz cavity in DCMS mode using balanced (red circles) and unbalanced (black squares) magnetic assemblies compared to the simulated profiles using the balanced (dashed red line) and unbalanced (solid black line) configuration. b) Distance from cavity surface to cathode surface central point (mm) plotted as a function of the cavity axis position.

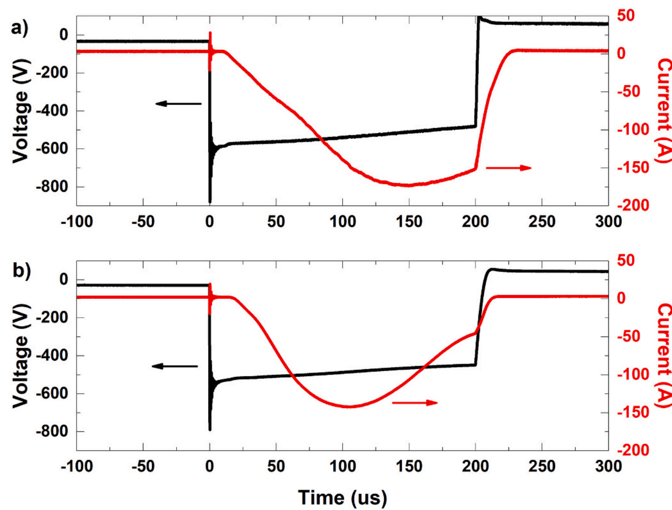

Fig. 10. Time resolved voltage (black) and current (red) waveforms for a HiPIMS discharge obtained with a grounded substrate using the a) balanced magnetic configuration and b) unbalanced 3-2-14 mm-SmCo magnetic configuration.

Fig. 6, and thus, less ions are available to participate to the sputtering. This is clearly seen on current waveforms shown in Fig. 10 where we can notice that, for a given power, in the unbalanced configuration the peak current intensity is reduced with respect to the balanced configuration.

Despite looking very similar, the coating profiles obtained in DCMS and HiPIMS with a balanced magnetic configuration and a grounded substrate exhibit a slight difference. As shown in Fig. 10 b) it appears that, for a given equatorial thickness, the peaks observed close to the iris of the cavity tend to decrease when using HiPIMS. It is even more obvious in the case of the unbalanced 3-2-14 mm-SmCo configuration. This suggests that the Nb ions flux at the equator is increased with respect to the one on the iris. The use of HiPIMS is thus already a way to reduce the thickness spread over the cavity inner surface with respect to the standard DCMS coating technique.

Nevertheless, the use of either a balanced or an unbalanced magnetic configuration does not give any significant difference when the substrate is kept at the ground potential. This type of observation was already reported on simpler sample geometries by Bohlmark et al. [13]. In their study, however, they focused on the increase of the magnetic field thanks to the use of a supplementary coil. In our geometry, this option is not applicable. We thus hereafter focus on the interest and use of a biasing voltage onto the substrate surface.

6.2. Biased substrate

We first notice that the use of unbiased HiPIMS, regardless of the magnetic configuration, leads to poor film density when the sample surface is not parallel to the cathode surface. This is shown in Fig. 12 using samples tilted with respect to the cathode. We clearly notice that a negative bias is the only lever available to densify the coated layer when dealing with complex geometries. It confirms that a dense layer can be obtained by applying a negative potential onto the substrate in order to properly attract the ions and induce a film growth which is not related to the tilt angle between the cathode and the substrate. We therefore explored the effect of the magnetic configuration when using biased substrates as this is a mandatory technique to use in order to elaborate dense and thus possibly Q-slope free films.

The cavity was maintained at −75 V throughout the entire coating process. This bias value was chosen to minimize the defect density in the Nb films and will be the subject of a further publication. The standard current and voltage temporal waveforms are shown in Fig. 13. We can notice that the bias current is higher for the unbalanced configuration which again confirms the enhanced ion flux at the cavity's surface with respect to the balanced configuration. The associated coating rate profiles as well as the normalized thickness profiles are displayed in Fig. 14a) and b), respectively. The first thing we can notice looking at Fig. 14 a) is that the application of a negative bias increases the coating rate with respect to the grounded configuration. The use of a biased balanced magnetic configuration improves the overall coating rate with a homogeneous increase all over the cavity profile. In addition, the use of an unbalanced 3–2-14 mm-SmCo magnetic configuration leads to a strong enhancement in the coating rate around the equatorial plane. We thus confirm the observation made in the last section of an increased ionic flow at the cavity surface in the unbalanced regime. Here, the application of a bias enhances the effectiveness of the collection of these species at the cavity surface through the established cathodic sheath and provides an efficient method for controlling the coating profile on our substrate.

Analysing Fig. 14 b) we can see how the film thickness is distributed along the cavity shape. It becomes obvious that the use of a balanced magnetic structure with or without biasing cannot help shaping the coating profile. Even though the absolute coating rate is increased by applying a bias, the thickness distribution remains similar to the grounded configuration. However, the use of an unbalanced magnetic configuration combined with the bias leads to a full redistribution of the

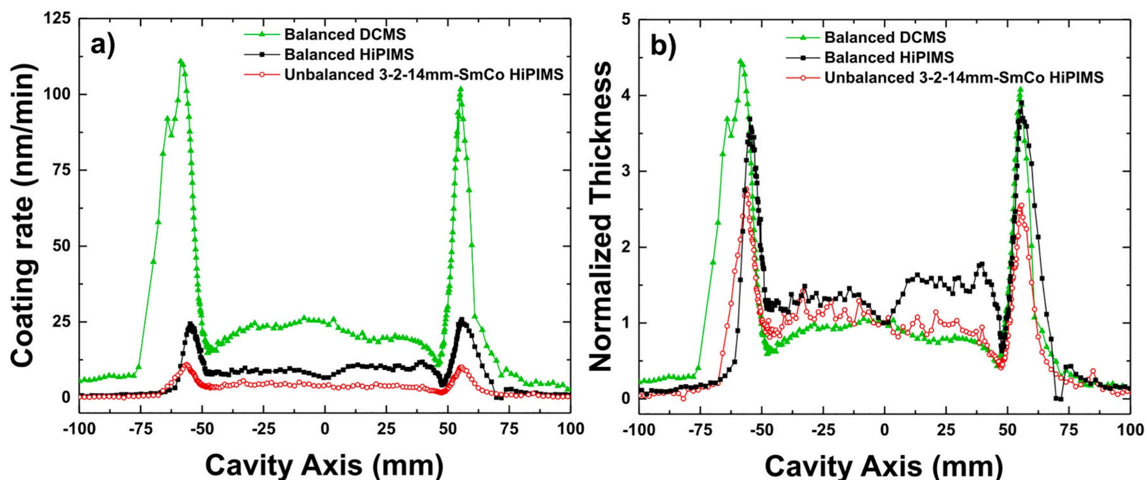

Fig. 11. Coating rates (a) and normalized thickness (b) profiles along the cavity axis for balanced DCMS (green triangles), balanced HiPIMS (black squares) and unbalanced HiPIMS (red circles) coatings. The normalization has been done with respect to the thickness measured at the equatorial position i.e., at 0 mm.

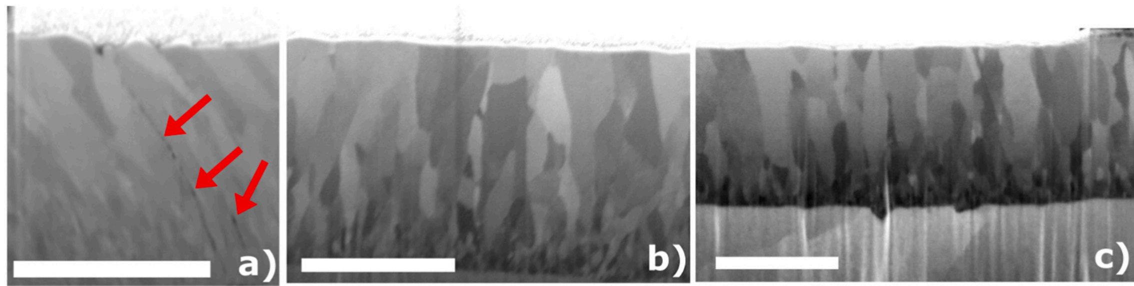

Fig. 12. Focused Ion Beam cross sections of Nb layers elaborated in balanced HiPIMS with a) 0 V, b) −50 V and c) −100 V bias on samples tilted at 45^0 with respect to the cathode surface. The scale bars represent 1um. The red arrows highlight the presence of porosities in the grounded substrate case.

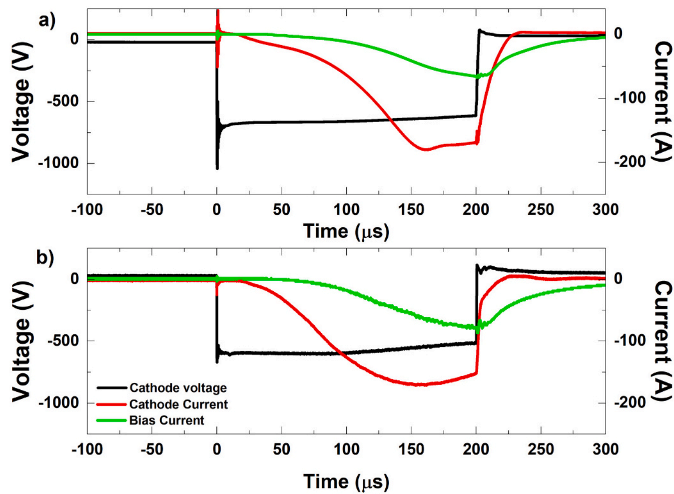

Fig. 13. Typical voltage and current waveforms for a biased HiPIMS discharge using a) a balanced magnetic configuration and b) an unbalanced 3-2-14 mm-SmCo magnetic configuration. The applied voltage bias is −75 V in continuous regime.

Nb layer onto the surface. The cavity can thus be coated with relatively thick layers without risking a peel-off due to a too important thickness spread.

We have validated that the use of an unbalanced and biased configuration is the way to go toward denser and more homogeneous layers in complex shapes. Looking carefully at the magnetic assembly, two other parameters can be further fine-tuned: the alignment of the magnetic poles with respect to the anodes and the magnetic strength of the assembly. We will discuss these two points in the following sections.

7. Magnetic pole location effect on the coating profile

One strategy that can be applied to tune the various species' fluxes at the surface of the cavity in the unbalanced case consists of controlling the magnetic flux lines that intercept the cavity surface by displacing the magnetic poles with respect to the anodes. The goal of this section is to assess whether using a different unbalanced configuration may result in a change in both the coating rate and the coating homogeneity on the cavity surface. A possible modification is the length of the central iron pole, as shown in Fig. 15. A long central pole, 14 mm, will allow the electrons to escape from the magnetic trap (in green) only through a very narrow channel (in teal), as seen in Fig. 15a), whereas the use of a short pole, 8 mm, will grant these electrons much more path probability toward the cavity surface (Fig. 15b). This effect is due to a different placement of the magnetic poles with respect to the anodes. The long pole configuration therefore corresponds to the one mentioned in the previous sections, 3-2-14 mm-SmCo, while the short pole assembly is the unbalanced 3-2-8mm-SmCo previously characterized in Table 1.

All the experiments with the new configuration were done in HiPIMS with a -75 V biased substrate. As reported in Fig. 16, we can first notice that the modification of the central iron pole length does not play an important role on the coating rates. However, a feature around the equatorial plane appears to change according to the pole length. Indeed, the use of an unbalanced source combined to a biased substrate leads to a small coating rate peak close to the equatorial position. As we reduce the pole length this peak spreads from about 15 mm wide, when using

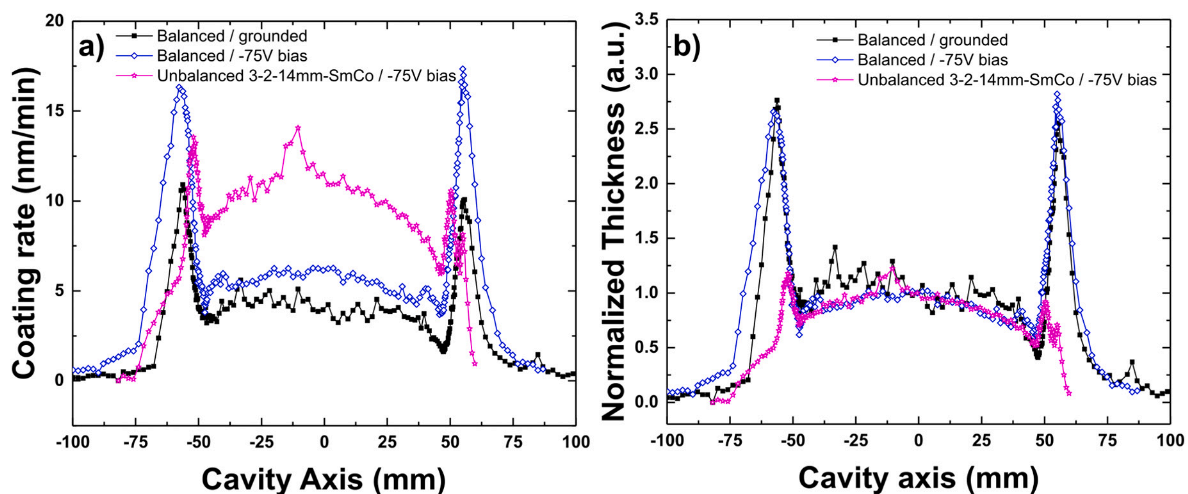

Fig. 14. a) Coating rate and b) relative thickness profiles obtained for HiPIMS coatings in balanced configuration with a grounded substrate (black squares), biased substrate (blue diamonds) and in the unbalanced 3-2-14 mm-SmCo biased configuration (magenta stars).

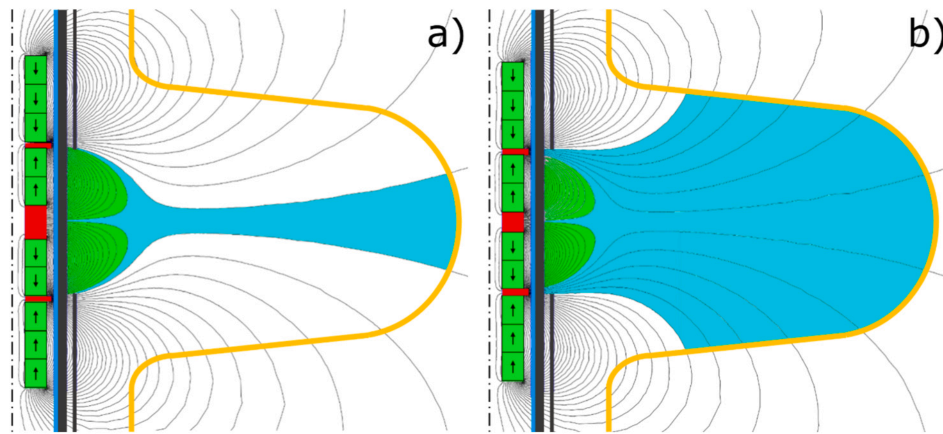

Fig. 15. Magneto-static simulations for the two versions of the unbalanced magnetic configurations with a) 14 mm and b) 8 mm central iron pole. The green area depicts the magnetic trap and the teal area the available escape paths for the electrons.

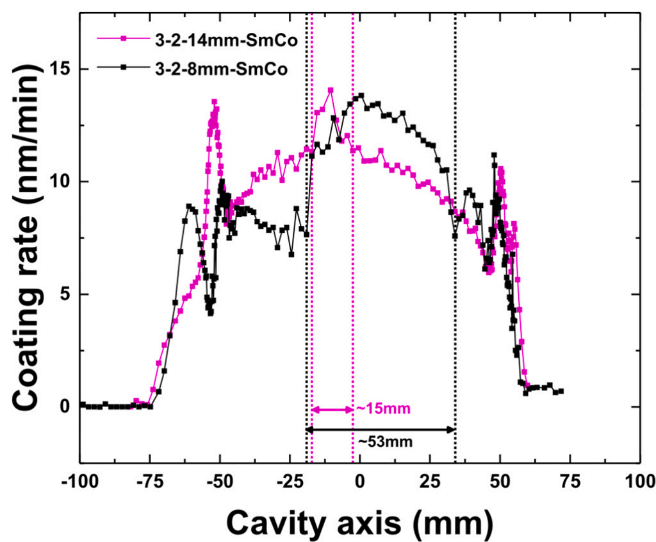

Fig. 16. Coating rates obtained with unbalanced magnetic configurations using either a 14 mm (magenta squares) or an 8 mm (black squares) central iron pole.

the 14 mm long pole, to 53 mm using the 8 mm long pole. As stated earlier, this can be explained by the spatial distribution of the field lines available for the electrons to escape from the magnetic trap. The lateral extension of the ionization region leads to the corresponding extension of the central coating peak. The control over the field lines distribution and their placement with respect to the anodes is thus of primary importance in order to tune on demand the coating profile on complex shapes.

As a comment, we can also add that the position of the magnetic poles with respect to the anodes must be as accurate as possible. In our case this appears to be the weak point of the system design as the central peak is never exactly located at the centre of the cavity. We are now investigating the possibility to build a new coating device that could eliminate this concern of magnet placement. As the use of a small iron pole helps redistributing the coating over the cavity surface, it could be of interest to study if this redistribution could be further enhanced by modifying the actual magnetic strength at the cathode surface.

8. Magnetic strength effect on the coating profile

In order to study the effect of the magnetic strength in the coating, we used two unbalanced magnetic configurations detailed before in Tables 1, 3-2-8mm-SmCo and 3-2-8mm-NdFeB, using two types of permanent magnets and a central iron pole of 8 mm. The calculated magnetic strengths at the cathode surface are shown in Fig. 17. As shown, the NdFeB magnets provide a higher magnetic strength to the respective assembly. The coatings were done in a similar fashion as in the previous section applying a −75 V bias to the substrate.

The as-deposited coating rates and thickness distribution profiles are reported in Fig. 18a) and b), respectively. The increase of the cathode surface magnetic field leads to a significant decrease in the coating rate by up to a factor of 2, as observed in previous studies [21] [22]. The overall coating distribution also appears to be smoothed as shown in Fig. 18b). The spike observed when using the NdFeB magnets, around 50 mm away from the cathode centre, is attributed to a slight misplacement of the magnetic assembly with respect to the cathode centre as discussed earlier.

9. Conclusion

We have observed that DCMS and HiPIMS coating techniques do not lead to fundamental differences in the coating profiles beyond the absolute coating rate, which is higher in DCMS, explained mainly by the recapture of metallic ions at the cathode surface. The use of an unbalanced magnetic configuration leads to a slight modification of the coating distribution in grounded HiPIMS with a reduction of the

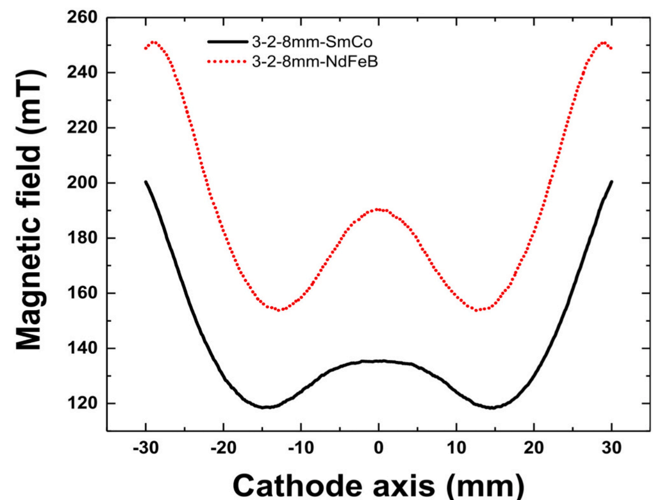

Fig. 17. Simulated magnetic field profiles at the cathode surface for unbalanced 3-2-8mm magnets using either SmCo (black line) or NdFeB (red dots) magnets.interpretation of the references to colour in this figure legend, the reader is referred to the web version of this article.)

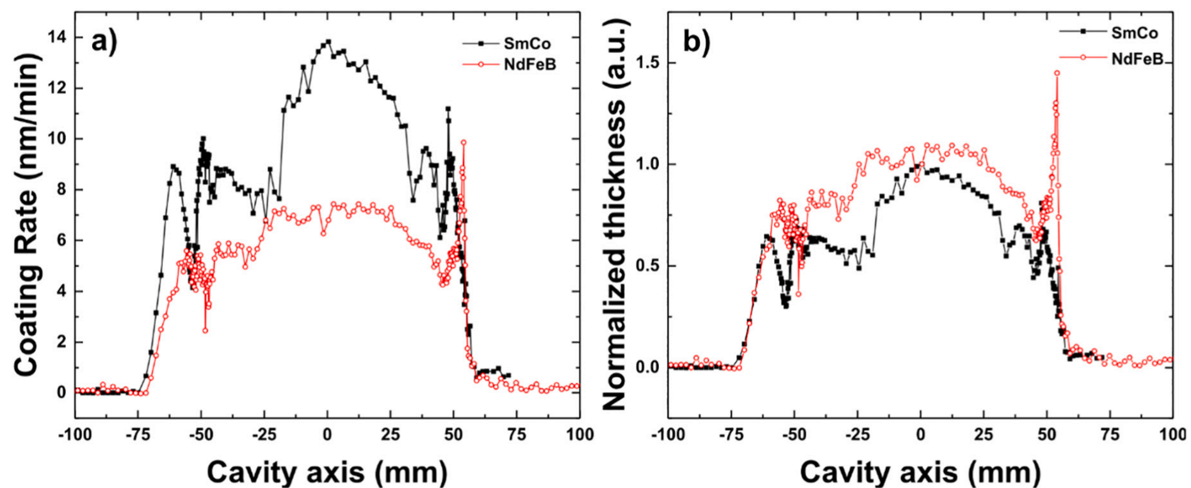

Fig. 18. a) Coating rate and b) normalized thickness profiles over the cavity surface for coatings performed using a biased unbalanced configuration with either SmCo (black squares) or NdFeB (red circles) magnets.

thickness spread over the cavity profile. The use of a negative bias on the cavity combined with an unbalanced magnetic source changes the layer thickness distribution by enhancing the capture of metallic ions at the sample surface through the established cathodic sheath. We have finally investigated the effect of the field lines spatial distribution that appears to be a driving factor for the spatial distribution of the discharge electrons and thus the shape of the ionization region. At last we improved even further the coating homogeneity by increasing the cathode surface magnetic field at the expense of a reduced coating rate.

In this paper we have thus demonstrated the possibility to:

1. Build magnetic assemblies that provide unbalanced characteristics to a cylindrical sputtering source.
2. Predict the shape of the ionization zone using a PICMC simulation code.
3. Tune the coating profile of an Nb layer deposited onto the internal surface of a complex shape using an unbalanced HiPIMS sputtering source combined with the application of a negative voltage onto the substrate to coat.

The use of such cylindrical unbalanced configuration is promising first in order to coat complex shapes objects and avoid peel-off that could arise from excessive coating thickness. A second interesting field of application would be the development of superconducting-insulating-superconducting (S-I-S) multilayer thin films for the use in SRF cavities as suggested by Gurevich [23] and Kubo [24]. A fundamental requirement of this technique is to control the films thickness ratio and thus to master the coating profile distribution in the cavities with the aim of reaching a profile as homogeneous as possible. Our study shows that a carefully designed magnetic stack has the capability of providing such homogeneity and would be a suitable solution to elaborate S-I-S thin films in an actual SRF resonator.

CRediT authorship contribution statement

Guillaume Rosaz: Conceptualization, Methodology, Formal analysis, Investigation, Writing – original draft, Writing – review & editing. **Aleksandra Bartkowska:** Investigation, Visualization, Writing – original draft, Writing – review & editing. **Carlota P.A. Carlos:** Investigation, Visualization, Writing – original draft, Writing – review & editing. **Thibaut Richard:** Software, Formal analysis, Validation, Visualization, Writing – original draft, Writing – review & editing. **Mauro Taborelli:** Supervision, Writing – original draft, Writing – review & editing.

Declaration of competing interest

The authors declare that they have no known competing financial interests or personal relationships that could have appeared to influence the work reported in this paper.

Acknowledgements

C. Pereira Carlos acknowledges the financial support provided by the Fundação para a Ciência e a Tecnologia, project SFRH/BEST/150601/2020.

References

[1] V. Arbet-Engels, C. Benvenuti, S. Calatroni, P. Darriulat, M.A. Peck, A.-M. Valente, C. Van't Hof, Superconducting niobium cavities, a case for the film technology, Nucl. Inst. Methods Phys. Res. A 463 (2001) 1–8.

[2] C. Benvenuti, N. Circelli, M. Hauer, Niobium films for superconducting accelerating cavities, Appl. Phys. Lett. 45 (5) (1984) 583.

[3] D. Boussard, E. Chiaveri, E. Haebel, H. Kindermann, R. Losito, S. Marque, V. Rodel, M. Stirbet, The LHC superconducting cavities, in: Proceedings of the 1999 Particle Accelerator Conference, New York, 1999.

[4] A. Miyazaki, W. Venturini Delsolaro, Two different origins of the Q-slope problem in superconducting niobium film cavities for a heavy ion accelerator at CERN, Phys. Rev. Accel. Beams 22 (2019), 073101, https://doi.org/10.1103/PhysRevAccelBeams.22.073101.

[5] W. Venturini-Delsolaro, K. Artoos, O. Capatina, Y. Kadi, Y. Leclercq, E. Montesinos, A. Miyazaki, V. Parma, G. Rosaz, K. Schirm, A. Sublet, S.Teixeira Lopez, M. Therasse, L. Williams, Lessons learned from the HIE-ISOLDE cavity production and cryomodule commissioning, in: 18th International Conference on RF Superconductivity, Lanzhou, 2017. https://accelconf.web.cern.ch/srf2017/papers/tuxaa02.pdf.

[6] P. Marchand, Superconducting RF cavities for synchrotron light sources, in: Proceeding of EPAC, Lucerne, 2004. https://accelconf.web.cern.ch/e04/PAPERS/MOYCH03.PDF.

[7] S. Posen, A. Romanenko, A. Grassellino, O.S. Melnychuk, D.A. Sergatskov, Ultralow surface resistance via vacuum heat treatment of superconducting radio-frequency cavities, Phys. Rev. Appl. 13 (1) (2020) 014024, https://doi.org/10.1103/PhysRevApplied.13.014024, 1.

[8] C. Benvenuti, S. Calatroni, I.E. Campisi, P. Darriulat, M.A. Peck, R. Russo, A.-M. Valente, Study of the surface resistance of superconducting niobium films at 1.5 GHz, Phys. C 316 (1999) 153–188.

[9] D. Tonini, C. Greggio, G. Keppel, F. Laviano, M. Musiani, G. Torzo, V. Palmieri, Morphology of niobium films sputtered at different target-substrate angle, in: 11th Workshop on RF superconductivity, Lübeck/Travemünder, 2003, 1, https://accelconf.web.cern.ch/SRF2003/papers/thp11.pdf.

[10] S. Calatroni, 20 years of experience with the Nb/Cu technology for superconducting cavities and perspectives for future developments, Phys. C 441 (2006) 95–101.

[11] C. Benvenuti, D. Boussard, S. Calatroni, E. Chiaveri, J. Tuckmantel, Production and test of 352MHz niobium sputtered reduced beta cavities, in: 8th Workshop on RF superconductivity, Abano Terme, 1997. https://accelconf.web.cern.ch/SRF97/papers/srf97d25.pdf.

[12] C. Benvenuti, P. Bernard, D. Bloess, G. Cavallari, E. Chiaveri, E. Haebel, N. Hilleret, J. Tuckmantel, W. Weingarten, Superconducting niobium sputter-coated copper cavity modules for the LEP energy upgrade, in: Conference Record of the 1991 IEEE Particle Accelerator Conference, 1991.
[13] J. Bohlmark, M. Östbye, M. Lattemann, H. Ljungcrantz, T. Rosell, U. Helmersson, Guiding the deposition flux in an ionized magnetron discharge, Thin Solid Films 515 (2006) 1928–1931, https://doi.org/10.1016/j.tsf.2006.07.183.
[14] H. Hajihoseini, M. Čada, Z. Hubička, S. Ünaldi, M.A. Raadu, N. Brenning, J. T. Gudmundsson, D. Lundin, Sideways deposition rate and ionized flux fraction in dc and high power impulse magnetron sputtering, J. Vac. Sci. Technol. A 38 (2020), 033009.
[15] D.C. Meeker, Finite element method magnetics, version 4.2 [Online]. Available: http://www.femm.info.
[16] A. Pflug, M. Siemers, T. Melzig, L. Schäfer, G. Bräuer, Simulation of linear magnetron discharges in 2D and 3D, Surf. Coat. Technol. 260 (2014) 411–416.
[17] Y. Yamamura, H. Tawara, Energy dependence of ion-induced sputtering yields from monoatomic solids at normal incidence, At. Data Nucl. Data Tables 62 (1996) 149–253.
[18] T. Richard, I. Furno, A. Sublet, M. Taborelli, Influence of ion induced secondary electron emission parameters in PICMC plasma simulations with experimental validation in DC cylindrical diode and magnetron discharges, Plasma Sources Sci. Technol. 29 (9) (2020), 095003, https://doi.org/10.1088/1361-6595/aba986.
[19] I.V. Svadkovski, D.A. Golosov, S.M. Zavatskiy, Characterisation parameters for unbalanced magnetron sputtering systems, Vacuum 68 (2002) 283–290.
[20] J. Emmerlich, S. Mráz, R. Snyders, K. Jiang, J.M. Schneider, The physical reason for the apparently low deposition rate during high-power pulsed magnetron sputtering, Vacuum 82 (2008) 867–870.
[21] H. Hajihoseini, M. Cada, Z. Hubicka, S. Unaldi, M.A. Raadu, N. Brenning, J. T. Gudmundsson, D. Lundin, The effect of magnetic field strength and geometry on the deposition rate and ionized flux fraction in the HiPIMS discharge, Plasma 2 (15) (2019).
[22] J.W. Bradley, A. Mishra, P.J. Kelly, The effect of changing the magnetic field strength on HiPIMS deposition rates, J. Phys. D. Appl. Phys. 48 (2015), 215202.
[23] A. Gurevich, Maximum screening fields of superconducting multilayer structures, AIP Adv. 5 (2015), 017112.
[24] T. Kubo, Multilayer coating for higher accelerating fields in superconducting radio-frequency cavities: a review of theoretical aspects, Supercond. Sci. Technol. 30 (2017), 023001.